Optics and Laser Technology 123 (2020) 105954

Contents lists available at ScienceDirect

Optics and Laser Technology

journal homepage: www.elsevier.com/locate/optlastec

Full length article

Direct laser interference patterning of stainless steel by ultrashort pulses for antibacterial surfaces

Alexander Peter[a], Adrian H.A. Lutey[b,*], Sebastian Faas[a], Luca Romoli[b], Volkher Onuseit[a], Thomas Graf[a]

[a] Institut für Strahlwerkzeuge, University of Stuttgart, Pfaffenwaldring 43, 70569 Stuttgart, Germany
[b] Dipartimento di Architettura e Ingegneria, University of Parma, Parco Area delle Scienze 181/A, 43124 Parma, Italy

HIGHLIGHTS

- Direct Laser Interference Patterning (DLIP) is performed on stainless steel.
- Periodic 'cones' and 'holes' with period ~850 nm are produced over areas of 250 mm^2.
- Textured surfaces are hydrophobic with a high peak density (S_{pd} = 1.56–1.9 peaks/μm^2).
- *E. coli* and *S. aureus* retention is reduced by up to 99.8% and 79.1%, respectively.
- Antibacterial properties are demonstrated over large surfaces textured by DLIP.

ARTICLE INFO

Keywords:
Direct laser interference patterning
Two beam interference
Ultrashort laser pulses
Functional surfaces
Antibacterial surfaces
Stainless steel

ABSTRACT

Direct Laser Interference Patterning (DLIP) with ultrashort pulses was exploited to produce tailored periodic sub-micrometer structures on stainless steel surfaces to reduce bacterial attachment and retention. Laser pulses with wavelength 1030 nm and duration 8 ps were employed to form a two-beam line interference pattern that was applied in a two-pass strategy to produce fine cross-wise surface structures with a period of ~ 850 nm and a depth of ~ 500 nm. The laser setup and process parameters were selected based on a simple theoretical model of the resulting interference pattern and ablation depth to limit the number of contact points available for bacterial cells with dimensions 500–2000 nm. Periodic 'cones' and 'holes' were produced covering areas of 250 mm^2 with the same interference pattern by exploiting the dependence of laser-induced periodic surface structures on polarization. Cones and holes yielded reductions in E. coli retention of 99.8% and 99.4%, respectively, and S. aureus retention of 70.6% and 79.1%, respectively, after two hours immersion in bacterial solution compared to reference samples. Such reductions achieved over large surface areas suggests that this approach is appropriate for upscaling and high throughput production of antibacterial metallic surfaces in the food and healthcare industries.

1. Introduction

Functional surfaces are of increasing interest in advanced manufacturing processes within the food and healthcare industries where products must meet higher quality and performance standards. Antibacterial stainless steel surfaces have much potential to prevent contamination, infection and the formation of biofilm with important consequences for consumers, workers and patients [1,2]. In the most critical of applications, harsh chemical cleaning agents such as sodium hydroxide or sodium hypochlorite are currently required to eliminate and prevent biofilms [3]. Functional surfaces that reduce bacterial retention are therefore of interest not only for minimizing contamination, but also for reducing cleaning requirements and associated downtime, corrosion, environmental impact and residual chemical content. A range of manufacturing methods such as plasma etching, anodic oxidation, chemical vapor deposition, lithography and electrospinning have been proposed to achieve antibacterial behavior by tailoring wettability and topography to minimize the interaction between bacterial cells and surfaces [4]. Antibacterial surfaces are often designed to mimic naturally occurring self-cleaning and antibacterial surfaces such as the lotus leaf and cicada wing, which are characterized by hierarchical superhydrophobic micro and nanoscale structures and

* Corresponding author.
E-mail address: adrian.lutey@unipr.it (A.H.A. Lutey).

https://doi.org/10.1016/j.optlastec.2019.105954
Received 8 July 2019; Received in revised form 25 October 2019; Accepted 11 November 2019
Available online 19 November 2019

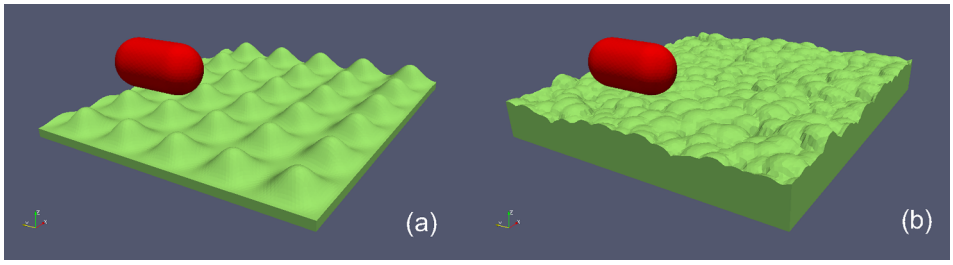

Fig. 1. Schematic of the interaction between a rod-like bacterial cell such as *Escherichia coli* and a textured surface for 'positive' surface features protruding above the mean plane (a) and 'negative' surface features penetrating below the mean plane (b).

densely-packed bactericidal nano-pillars, respectively [5,6]. The importance of surface topography and hydrophobicity on bacterial retention has been the subject of extensive investigations [7–9], with the former found to be of strong influence where the characteristic feature size is smaller than the bacterial cell dimensions, thus minimizing the number of contact points between the cell and substrate. This concept is represented schematically in Fig. 1 for a rod-like bacterial cell such as *Escherichia coli* interacting with 'positive' and 'negative' surface features smaller than the cell size, protruding above and below the mean plane respectively.

The recent demonstration of ultrashort-pulse laser-textured antibacterial surfaces has driven investigations into productive laser-based techniques for the generation of suitable surface structures over large areas relevant to industrial applications [10–13]. Both surface topography and wettability can be modified by ultrashort pulsed laser irradiation in a single-step process [14–16]. Further to spatial concentration of the focused laser beam, processing of metals with ultrashort pulses provides energy deposition on a time-scale shorter than the electron–phonon relaxation time, provoking strong electron excitation, non-equilibrium thermodynamic responses [17] and self-reorganization of the surface topography. Interaction between linearly polarized laser pulses and surface plasmon polaritons can produce laser-induced periodic surface structures (LIPSS) perpendicular to the polarization orientation with a ridge separation in the order of the laser wavelength at low fluence and larger hierarchical structures such as bumps and spikes with superimposed LIPSS at high fluence [18,19]. LIPSS having two-dimensional symmetry (2D-LIPSS) can be produced with double-pulse irradiation over large areas [20]. Depending on the irradiation configuration and the material, rhombic [21], triangular [22], dot [23] and square [24] structures can be attained.

Direct laser interference patterning (DLIP) is an alternative method for producing micro and nanoscale structures on metallic, semiconductor and polymer surfaces, providing greater flexibility in the choice of target material and surface texture. In contrast to LIPSS, this method exploits direct material removal by ablation to produce a predefined surface topography. In principle, a number of overlapping coherent beams are employed to produce a periodic interference pattern on the material surface, with a given spatial variation of the fluence resulting in corresponding material removal on the target surface [25–28]. The number of interfering beams, their polarization and choice of processing parameters provide a great variety of possible configurations [29–31]. The use of ultrashort laser pulses for DLIP limits unwanted melting effects and can produce diverse structures through the interplay between DLIP and LIPSS [32]. These aspects, in turn, allow greater flexibility compared to other methods, promising more controlled generation of functional surfaces appropriate for minimizing bacterial retention. It has been shown that DLIP can be employed to reduce bacterial attachment on copper, titanium and polymeric surfaces [33–37]. Many current industrial applications in the food and healthcare industries, however, require the use of stainless steel and the texturing of very large areas, suggesting that further research must be undertaken into the use of this material and ultrafast Yb:YAG laser sources emitting at 1030 nm, which show great promise for high-power (> 1 kW) processing [38–40].

The focus of the current work therefore lies in the generation of submicrometer surface structures over large areas on stainless steel samples by DLIP using 8 ps laser pulses at a wavelength of 1030 nm. Two-dimensional surface structures have been produced over an area of 250 mm^2 with a two-beam line interference pattern and a perpendicular crosswise structuring strategy. The structures were designed to guarantee isotropic properties and minimize the number of available contact points for bacterial cells during the initial phases of attachment. The setup was chosen based on a simple process model using Beer-Lambert's absorption law to predict the ablated volume and surface topography resulting from a given DLIP interference pattern and laser parameters [41,42]. The influence of LIPSS was also exploited to achieve different periodic structures, allowing investigation into the effects of 'positive' and 'negative' surface structures (Fig. 1). The resulting stainless steel surfaces were analyzed with scanning electron microscopy (SEM), shear-force microscopy (ShFM) and the sessile drop method to determine their form, topography and wettability, and allow comparison between experimental and theoretical results in the context of existing design guidelines for laser-textured antibacterial surfaces [43]. Bacterial retention tests were then performed on laser-textured and untextured control specimens with *Escherichia coli* (*E. coli*) and *Staphylococcus aureus* (*S. aureus*) bacterial cells to quantify the antibacterial performance of each textured surface.

2. Materials and methods

2.1. Materials

All DLIP experiments were performed by texturing the entire surface of 50 mm × 50 mm mirror-polished 316L stainless steel specimens with an initial average areal surface roughness of 30 nm. Control samples for bacterial retention tests were of the same material with an average areal surface roughness of 0.37 µm, representing current industrial food handling practices [44].

2.2. DLIP laser setup

The setup employed for surface structuring by DLIP was capable of combining up to four beams while varying the period of the interference pattern, spot diameter on the sample surface and individual polarization of each beam. Full details of the arrangement have been presented in [45]. In contrast to interference patterns obtained with a greater number of beams, a two-beam configuration is advantageous in terms of contrast, smaller periods and phase stability [46]. An additional advantage is provided in the case of multi-pulse processing of moving workpieces, whereby positioning inaccuracies parallel to the interference lines have no influence on the resulting topography. This property is beneficial for large-area surface structuring where components must be continuously moved relative to the laser beam.

In principle, the setup worked as follows: the laser beam was first launched from above through a variable telescope and then split by a diffractive beam splitter into two beams with a total angle of 18.6°

between the beams. Two inner mirrors guided the beams through half-wave plates to allow independent variation of the polarization of each. Two subsequent mirrors reflected the beams to one spot on the sample surface where the interference pattern was formed. The outer mirrors were mounted on mechanical goniometers to allow variation of the angle of incidence and therefore control of the period of the interference pattern on the textured surface. The sample was held on a stage with numerically controlled axes, providing movement for structuring over an area of up to 800 mm × 900 mm.

2.3. Generated interference pattern

The intensity distribution $I(x, y)$ of two coherent interfering beams is described by [25]

$$I(x, y) = 2I_0\left[1 + \cos\left(\frac{4\pi\sin(\theta)}{\lambda}x\right)\right] \quad (1)$$

where I_0 is the intensity of each of the two incident laser beams having top-hat distributions on the target surface, λ the wavelength, and θ the angle of incidence on the surface. This formula is based on the assumption that both beams have the same intensity, polarization and angle of incidence in a plane of incidence parallel to the x-direction.

To consider the ablation process with pulsed laser beams have Gaussian intensity profiles, Eq. (1) can first be supplemented with a Gaussian cross section

$$I(x, y) = 4I_0\exp\left[-2\left(\frac{4x^2}{d_x^2} + \frac{4y^2}{d_y^2}\right)\right]\cdot\left[1 + \cos\left(\frac{4\pi\sin(\theta)}{\lambda}x\right)\right] \quad (2)$$

where d_x and d_y are the diameters of the Gaussian beam for one DLIP pixel in the x- and y-directions at the level of $1/e^2$.

In terms of the Gaussian temporal shape of the laser pulse, the intensity distribution can then be transformed into the fluence distribution of one DLIP pixel by multiplying $I(x, y)$ with the full width half maximum (FWHM) pulse duration, τ_p

$$\phi_{inc}(x, y) = I(x, y)\cdot\tau_p/0.94 = 2\phi_m\cdot\exp\left[-2\left(\frac{4x^2}{d_x^2} + \frac{4y^2}{d_y^2}\right)\right]\cdot\left[1 + \cos\left(\frac{4\pi\sin(\theta)}{\lambda}x\right)\right] \quad (3)$$

where the mean fluence is

$$\phi_m = 4E_p/(\pi d_x d_y) \quad (4)$$

and E_p is the pulse energy incident on the surface. The peak fluence, $\phi_{inc,max}$, is four times the mean fluence due to the Gaussian distribution and maximum interference between the two beams. The period

$$\Lambda = \frac{\lambda}{2\sin(\theta)} \quad (5)$$

of the interference pattern depends on the angle of incidence θ and the wavelength λ [25].

Based on investigations performed in [9], the characteristic feature size of laser-textured antibacterial surfaces must be similar or smaller than the size of a bacterial cell. Of the bacteria types considered within this work, *E. coli* is cylindrical in shape with a length and diameter of 2 µm and 500 nm, respectively, and *S. aureus* is spherical in shape with a diameter of 500 nm. A structure period of 850 nm was therefore chosen to achieve a half-period feature size smaller than 500 nm. With a wavelength of 1030 nm, this period required an angle of incidence of 37° according to Eq. (5).

Fig. 2 shows a comparison between the calculated interference pattern obtained with this angle of incidence and that recorded with a beam camera under the same conditions. The theoretical results shown on the left-hand side were calculated according to Eq. (3), while the recorded fluence distribution achieved with the DLIP setup is shown on the right. The experimental interference pattern was magnified with a 50 × microscope objective and recorded with a camera chip with a pixel size of 8.3 µm. The measured results agree well with the calculated fluence distributions.

2.4. Microscopy and analysis of the topography

Textured samples were analyzed with a JEOL JSM-6490LV scanning electron microscope (SEM) to determine the size, form and homogeneity of the produced surface structures. The surface topography was quantified with shear-force microscopy (ShFM), a non-contact scanning probe microscopy technique. The ShFM setup, described in detail elsewhere [47], provided topography maps of the measured surfaces with a resolution of 0.1 nm and 1 nm in the vertical and horizontal directions, respectively, over an area of up to 100 µm × 100 µm. A custom setup was employed comprising a quartz tuning fork, tungsten wire probe with a tip diameter of 50 nm, three-axis nano-positioner and controller. This arrangement allowed large sample travel distances and did not suffer from artefacts due to scattering of stray light from the textured surface. Data acquired by ShFM was utilized to determine the average areal surface roughness, skewness, kurtosis and density of peaks of all surfaces in line with their standard definitions given in ISO 25178 [48].

2.5. Wettability analysis

The static water contact angle and sliding angle of laser-textured samples were quantified with the sessile drop method after a 30-day ageing period in ambient air. This ageing period was introduced to ensure that any potential transition from a hydrophilic to a hydrophobic state [14,49,50] was complete prior to measurement of the wettability and antibacterial performance. Wettability measurements were performed with a Dataphysics Instruments OCA20 goniometer, deionized water droplets of volume 6 µL and a syringe of diameter 310 µm. The sliding angle, defined as the angle at which the droplet no longer adhered to the surface [52], was determined utilizing a rotation rate of 1°/s. DataPhysics SCA20 software was used to process images of the deposited droplets and quantify the static contact angle using Laplace-Young fitting of the droplet geometry.

2.6. Bacterial retention

Bacterial retention was quantified for three identical laser-textured samples of dimensions 50 mm × 50 mm and three untextured control samples of the same size for each surface structure and bacteria type. The method employed for assessing bacterial retention, presented in detail in [13], was based on ISO 22196 and ISO 27447 for measurement of antibacterial performance [53–54]. Bacterial solutions were firstly prepared by separately transferring *E. coli* (ATCC 8739) and *S. aureus* (ATCC 6538P) strains to Nutrient Agar (NA) and incubating for 24 h at 37 °C before transferring to NA again and incubating at the same temperature for an additional 18 h. This process was undertaken in conformance with ISO 27447 to ensure that the bacterial cells were free from environmental stresses and in an appropriate growth stage. The stock was then diluted to 1/500 with an optical density of 0.5 and transferred into separate sterilized containers with a volume of 200 mL. The cell density of the resulting solutions was 2.6×10^7 cfu/ml for *E. coli* and 8.2×10^6 cfu/ml for *S. aureus*. Laser-textured and control samples were individually cleaned for 15 min in acetone, sterilized for 10 min in pure ethanol and dried in air for 10 min in a UV hood prior to being transferred into separate containers with the bacterial solutions. The samples were held in a horizontal position with the laser-textured surface facing upwards for two hours at 24 °C while the containers were agitated at a frequency of 1.5 Hz and a stroke of 30 mm to facilitate contact between the bacterial cells and the surface. The samples were then removed from the containers and excess liquid eliminated by holding the samples in a vertical position for 2 min. Swabs were then taken in both orthogonal directions along each surface prior to seeding

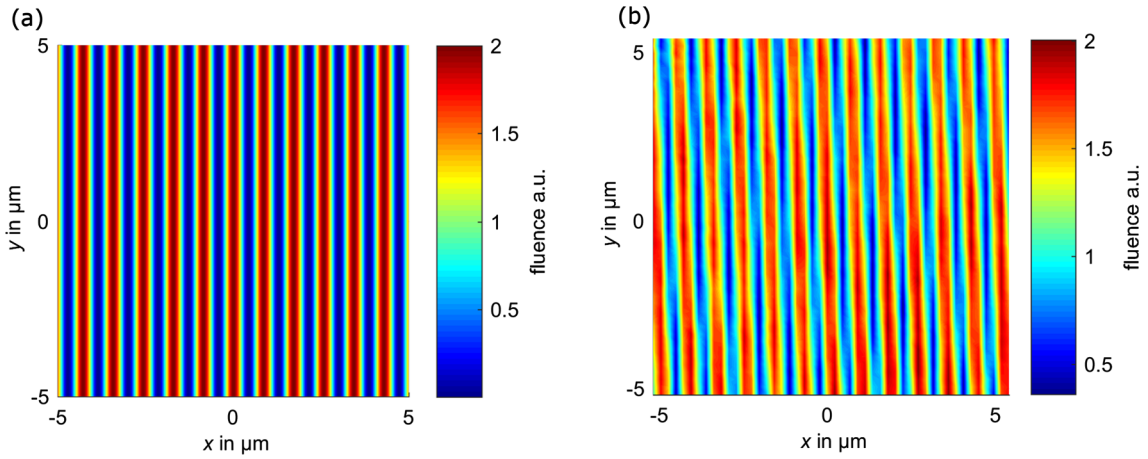

Fig. 2. Calculated (a) and recorded (b) interference patterns with two coherent beams and an angle of incidence of 37°.

in NA and incubating for 48 h at 37 °C. A colony counter was then employed to quantify the number of colony forming units per swab.

3. Results and discussion

3.1. Selection of process parameters and structuring strategy

An ablation model based on the Beer-Lambert absorption law was employed [41,42,55] to predict the topography of the ablated surface. Due to the Gaussian profile of the laser beams, together with continuous feed of the workpiece at v_y in y-direction and a repetition rate of f_{rep}, the ablation depth was expressed as the sum of Gaussian spatial intensity-dependent ablation events:

$$d(x, y) \simeq -\delta \sum_{i=-\infty}^{\infty} \ln\left(\phi_{inc}\left(x, y - i \cdot \frac{v_y}{f_{rep}}\right)/\phi_{th}\right) \quad i \in \mathbb{Z} \tag{6}$$

where δ is the energy penetration depth and ϕ_{th} the material ablation threshold. All positive values were set to zero since no ablation was expected to take place where the fluence was below the ablation threshold.

For mirror-polished stainless steel, ablation takes place when the incident fluence on the workpiece exceeds the threshold value of $\phi_{th} = 0.1$ J/cm^2. This value was obtained with the method described in [56]. The ablation threshold of stainless steel derived in this way was found to be similar to that given in the literature for steel, which has been reported as being slightly higher than 0.1 J/cm^2 in [57] and slightly lower than 0.1 J/cm^2 in [58] for approximately 60 pulses.

Figs. 3(a) and 4(a) show the targeted three-dimensional topography and a horizontal section, respectively, as calculated using Eq. (6) for the interference pattern shown in Fig. 2(a) and the processing parameters given in Table 1. With these parameters, the ablated grooves were calculated as having the same width as the ridges and a depth of about 0.5 µm. This depth was chosen to obtain a groove aspect ratio of about 1. Fig. 3(b) (3D) and Fig. 4 (2D horizontal and diagonal sections) show the calculated topography after a second, perpendicular processing step as part of a cross-wise strategy described below. It should be noted that the horizontal section in Fig. 4(a) applies to both one and two processing steps, as this region was not altered during the second step. Taking into account the increased surface roughness formed with the first pass (see Fig. 3(a)) the ablation threshold was estimated to be $\phi_{m2} = 0.05$ J/cm^2 during the second pass [59].

In order to structure large areas, a strategy with continuous feed parallel to the interference lines was applied to maximize the structuring rate. Heat accumulation effects during DLIP have been investigated for nanosecond laser pulses [60]; however, there have been no investigations of this type to date for picosecond pulses to the authors' knowledge. The repetition rate was therefore set to $f_{rep} = 100$ kHz to avoid significant heat accumulation effects. Under these conditions, heat accumulation was not considered to be significant based on the theory described in [61].

Due to the angle of incidence of the two beams and angular dispersion effects from the diffractive beam splitter, the area of the beam profile on the sample's surface had an elliptical shape, which was always elongated in x-direction, perpendicular to the interference lines and the feed direction. Angular dispersion was caused by the relatively

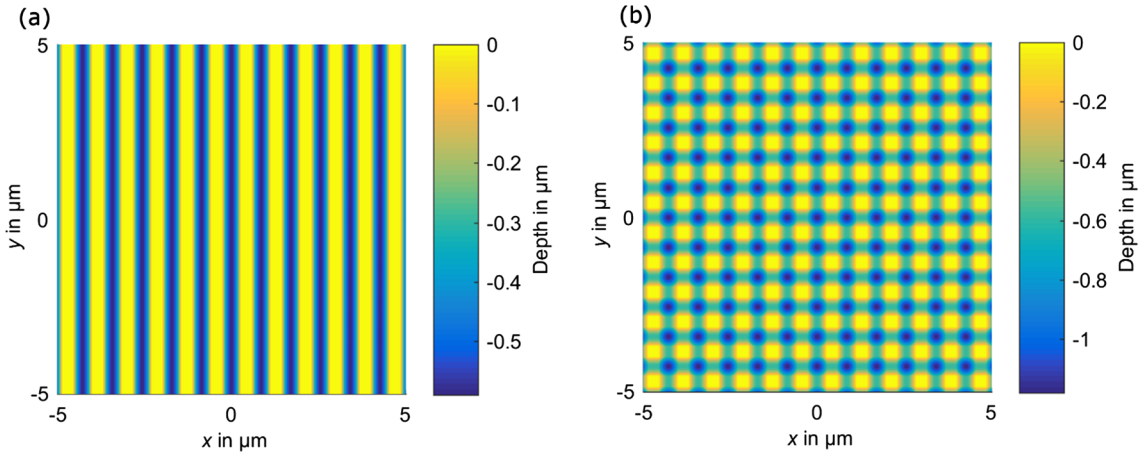

Fig. 3. Calculated topography after the first ablation process (a) and the second ablation process (b).

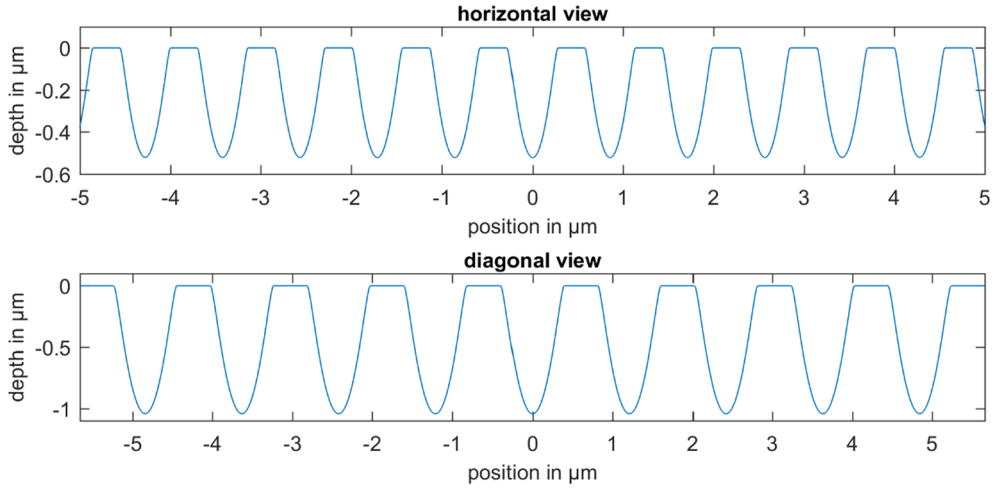

Fig. 4. Horizontal view (top) and diagonal view (bottom) of the calculated depth after the second ablation process.

Table 1
Process parameters employed for ablation calculation.

Parameter	Name	Value
δ	Energy penetration depth	9 nm [55]
ϕ_{th}	Material ablation threshold	0.1 $\frac{J}{cm^2}$
ϕ_m	Mean fluence incident on workpiece during 1st pass	0.1 $\frac{J}{cm^2}$
ϕ_{m2}	Mean fluence incident on workpiece during 2nd pass	0.05 $\frac{J}{cm^2}$
θ	Angle of incidence	37°
λ	wavelength	1030 nm
d_x	Beam diameter on workpiece in x-direction	190 μm
d_y	Beam diameter on workpiece in y-direction	60 μm
v_y	Feed rate	100 mm/s
f_{rep}	Repetition rate	100 kHz

broad spectral bandwidth of the laser and the diffractive beam splitter. For the performed experiments, the elongated diameter was 190 µm in the x-direction and 60 µm in y-direction. The spot diameters were determined according to [56].

Two-dimensional structures were obtained with the line interference pattern by adding a second process step in which the surface was rotated by 90°, as shown schematically in Fig. 5. Due to the dependence of optical absorption on surface roughness [59,62], the pulse energy used during the second processing step was reduced to half of that applied in the first step, leading to a balanced topography in the x- and y-directions. Fig. 3(b) shows the theoretically predicted topography formed by the two process steps. Due to uncertainties concerning the behavior of various physical quantities during the process such as the absorptivity and ablation threshold of the material, the employed parameters were based on values from the literature and were considered as an initial estimate.

3.2. Parametric study

Fig. 6 shows SEM images of the resulting topographies produced after the first process step with different pulse energies, E_p, corresponding to different mean fluences, ϕ_m. The remaining process parameters were set as estimated in the previous section (Table 1). Due to measurement uncertainties in determining the laser spot size, target ablation threshold and laser power, factors that can have a strong effect on experimental results, the ratio of peak fluence to the ablation threshold was set experimentally. This ratio represents the argument of the logarithm in Eq. (6). The pulse energy was firstly set to the minimum at which an ablation effect was observed (7.2 µJ). The resulting surface morphology is shown in the SEM image in Fig. 6(a). In this case, the ratio is 1 in Eq. (6) since the peak fluence is equal to the ablation threshold. For tests performed in section 3.1, the required ratio was instead 4:

$$\phi_{inc,max}/\phi_{th} = 4\phi_m/\phi_{th} = 0.4/0.1 = 4 \quad (7)$$

To achieve this value, the pulse energy was increased by a factor of four (29 µJ) compared to the minimum pulse energy exhibiting an ablation effect. The resulting morphology, which was applied for the final structures, is shown in Fig. 6(c). Fig. 6(b) instead shows the resulting

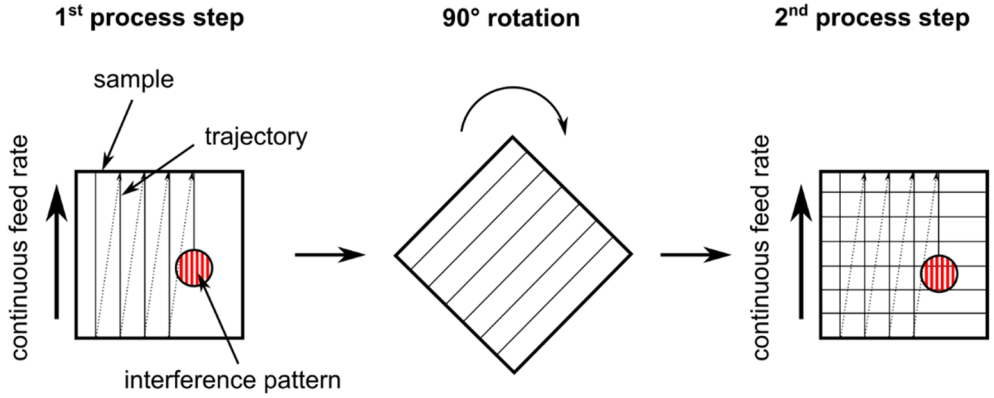

Fig. 5. Large area processing strategy for 2D structures with the 1D interference pattern. The lines of the interference pattern are always parallel to the direction of the feed. Lateral displacement of feed lines was 140 µm (30% overlap).

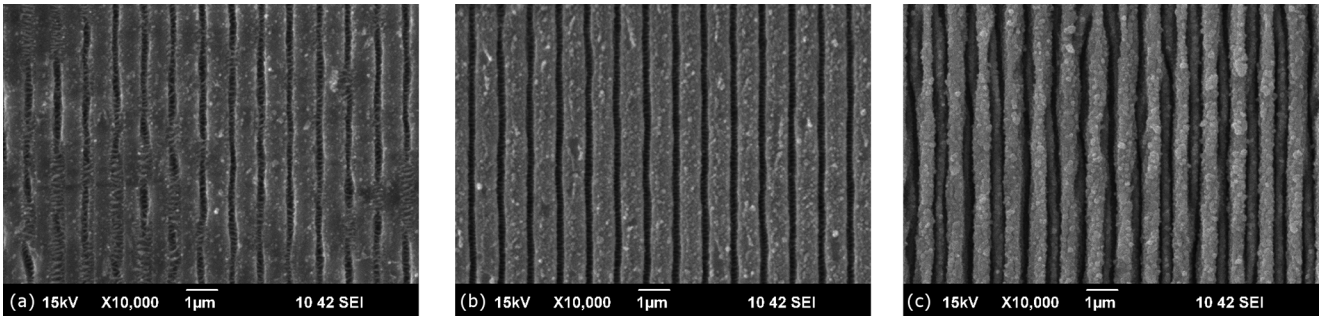

Fig. 6. SEM images of topographies produced with different pulse energies: $E_p = 7.2\mu J$ (a), $E_p = 9\mu J$ (b) and $E_p = 29\mu J$ (c).

topography when the pulse energy was calculated based purely on the parameters given in Table 1 (9 μJ). In this case, the width of the grooves is not as wide as the ridges, which is not in agreement with predicted values given by Eq. (6). This result is due to uncertainties in the spot size, laser power and ablation threshold. By setting the ratio of peak fluence to the ablation threshold experimentally, and therefore excluding uncertainties in these input parameters, good alignment was achieved between the predicted and experimental topography for all applied pulse energies.

The parameters used for production of the final topographies were the angle of incidence θ, feed rate v_y and repetition rate f_{rep} as listed in Table 1 and the pulse energy for the first pass (29 μJ) and second pass (14.5 μJ) to reach the required ratio of 4 according to Eq. (6). The hatch distance was 140.3 μm, a multiple of the structural period and a line overlap of about 26%. The throughput of the process was 7 mm^2/s, considering only the laser on time.

3.3. Topography analysis

In the case of two-beam DLIP, the fluence distribution of the interference pattern is limited to lines such as those shown in Fig. 2(a), which are independent of the polarization orientation. LIPSS resulting from material response to intense laser irradiation, however, arise perpendicular to the polarization orientation and have a period similar to the laser wavelength [16,18], leading to interplay between DLIP and LIPSS [32]. This dependence was exploited to achieve two different topography types, with parameters from sections 3.1 and 3.2 employed for processing in both cases. With *p*-polarization, LIPSS developed parallel to the interference lines. The resulting morphology corresponded to the calculated ablation geometry after the first process step (Fig. 7(a)) and 'cones' after the second process step (Fig. 7(b)). With *s*-polarization, LIPSS developed perpendicular to the interference lines, resulting in 'holes' after the first (Fig. 7(c)) and second process steps (Fig. 7(d)). In this case, the structures deviated from the calculated geometry and could not be described by Eq. (6). Both regular structures had a period of approximately 850 nm, which was consistent with the period predicted by the ablation model.

The primary characteristic features of both surfaces were similar in size to *E. coli* and *S. aureus* as intended, while finer features could also be seen on both textured surfaces in the form of nano-spheres and nano-ripples. The formation of these finer details was likely due to re-deposition of ablation products [67], microfluidic movement of molten material [32] and oxidation effects from contact with air during laser processing. The hierarchical nature of the laser-textured surfaces mimicked naturally occurring self-cleaning and antibacterial surfaces to some extent [5,6].

ShFM topography maps of the laser-textured surfaces are shown in Fig. 8. The corresponding roughness parameters are listed in Table 2. Comparing the topography of the cones in Fig. 8(a) with the calculated profile in Fig. 3(b), it is evident that the measured ablation depth is slightly lower than the theoretically predicted value. This effect may be attributed to differences between the modelled and actual fluence distribution, re-deposition of ablation products and oxidation effects. Positioning inaccuracies perpendicular to the feed direction, which could not be avoided, may have also contributed to this deviation. The measured surfaces are highly regular, with an average areal surface roughness of 55 nm for the cones and 68 nm for the holes, marginally higher than that of the original mirror-polished samples (30 nm). The skewness is low while the kurtosis is close to 3 in both cases, indicating symmetrical and wide height distributions. The density of peaks, an important factor indicating the quantity of available contact points for bacterial cells, is above 1 μm^{-2} for both cones and holes structures. A large reduction in available contact points is expected once the density of peaks exceeds the theoretical cell density [13]. In the case of *E. coli*, cylindrical in shape with a length of 2 μm and diameter of 500 nm, a reduction in contact points is therefore expected where the density of peaks is greater than 1 μm^{-2}, which was attained on both textured surfaces. In the case of *S. aureus*, spherical in shape with a diameter of 500 nm, the equivalent threshold is 4 μm^{-2}, which was not attained on either textured surface. The presence of fine nano-scale features is nonetheless expected to further influence bacterial attachment and biofilm formation.

3.4. Wettability analysis

The average static water contact angle of the laser-textured surfaces was 154 ± 3° and 148 ± 5° for cones and holes, respectively. Images of deposited water droplets on both surfaces are provided in Fig. 9. Droplet sliding was not observed for angles up to 90°. The laser-textured surfaces were therefore considered hydrophobic, as the static contact angle was greater than 90° [63], but not superhydrophobic due to lack of droplet sliding [64]. The surfaces nonetheless exhibited considerably lower wettability than untextured 316L stainless steel, which is characterized by a static water contact angle of 77 ± 3° [50]. The higher static water contact angle of laser-textured surfaces can partially be attributed to chemical changes taking place after laser irradiation, resulting in changes in the intrinsic wettability of the fluid-substrate combination. Though the evolution of wettability was not investigated during the 30-day ageing period, transition from a hydrophilic to a hydrophobic state over a period of up to 30 days after ultrashort pulse laser exposure has been extensively investigated in the literature [49,50]. Kietzig et al. [14] proposed that such a transition is due to the formation of active magnetite following laser exposure and subsequent dissociative adsorption of carbon dioxide from the air. The transition has been shown to be accompanied by a reduction in oxygen content and an increase in carbon content on the surface [50].

The increase in static water contact angle on the laser-textured surfaces is also due to the resulting surface topography, where an increase in the ratio of the actual to projected surface area leads to a higher apparent contact angle for intrinsically hydrophobic fluid-substrate combinations [51]. It has been shown that relatively high laser energy doses are required to achieve superhydrophobic surfaces characterized by droplet sliding through the formation of larger hierarchical structures [50]. In the present study, however, the aim was to prioritize

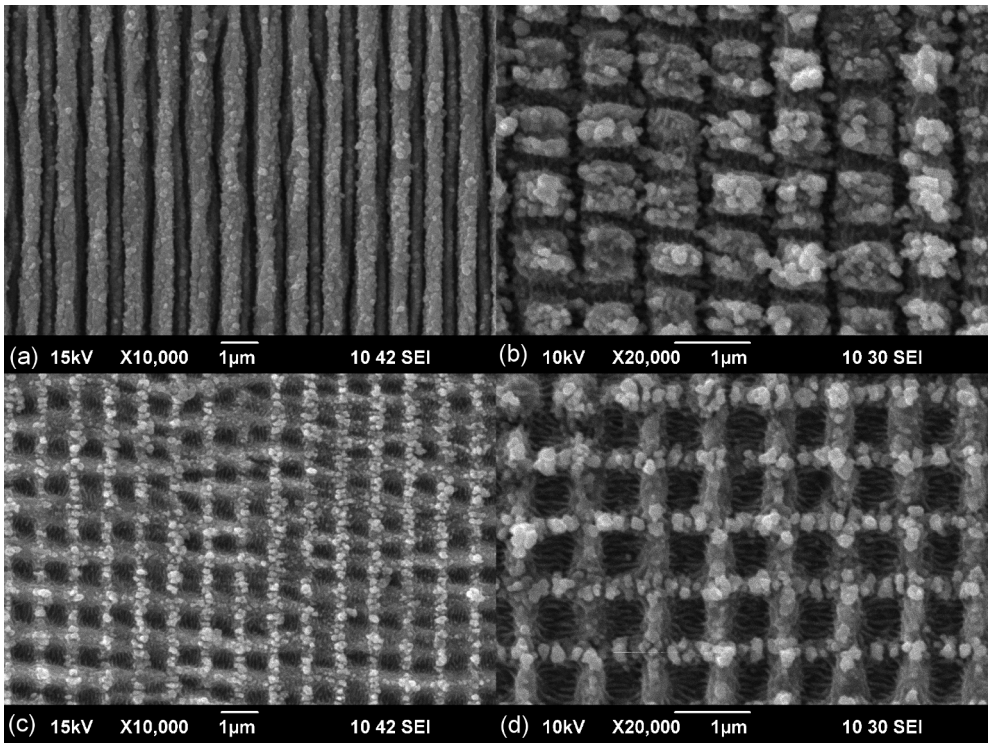

Fig. 7. SEM images of structures produced with *p*-polarization after the first process step (a) and second process step (b). SEM images of structures produced with *s*-polarization after the first process step (c) and second process step (d). The resulting topographies are cones (b) and holes (d). The magnification is 10000× (left) and 20000× (right).

sub-micrometer surface features, as large reductions in bacterial attachment have been shown to take place where the feature size is smaller than bacterial cells [9–13,15]. Lower wettability has nonetheless been associated with lower bacterial attachment independent of surface topography [8,13,65,66], for which this factor was expected to further reduce bacterial attachment and biofilm formation.

3.5. Bacterial retention

Fig. 10 shows geometric averages of the residual bacteria count on laser-textured samples after two hours of exposure to the bacterial solutions, normalized against 316L stainless steel control samples with an average areal surface roughness of 0.37 μm. Values represent the number of residual colony forming units determined with a colony counter after sample swabbing and subsequent incubation. The laser-textured surfaces exhibit large reductions in *E. coli* retention (99.8% and 99.4% for cones and holes, respectively) and moderate reductions in *S. aureus* retention (70.6% and 79.1% for cones and holes, respectively) compared to the control samples. The fine surface features resulting from ultrashort pulsed DLIP are clearly well-suited to reducing *E. coli* attachment and retention. The high density of peaks of the laser-textured surfaces, above 1 μm^{-2} for both cones and holes, is of fundamental importance in achieving this result, and is in line with other works that have demonstrated reductions in *E. coli* attachment on laser-textured surfaces [10,13]. *S. aureus* is likely to have been more greatly influenced by the lower wettability of laser-textured surfaces. In this

Table 2
Topography parameters for cones and holes produced by ultrashort pulsed DLIP.

Parameter	Cones	Holes
Areal roughness, S_a	55 ± 1 nm	68 ± 1 nm
Skewness, S_{sk}	0.004 ± 0.02	−0.09 ± 0.02
Kurtosis, S_{ku}	3.08 ± 0.02	2.74 ± 0.02
Density of peaks, S_{pd}	1.6 ± 0.2 μm^{-2}	1.9 ± 0.2 μm^{-2}

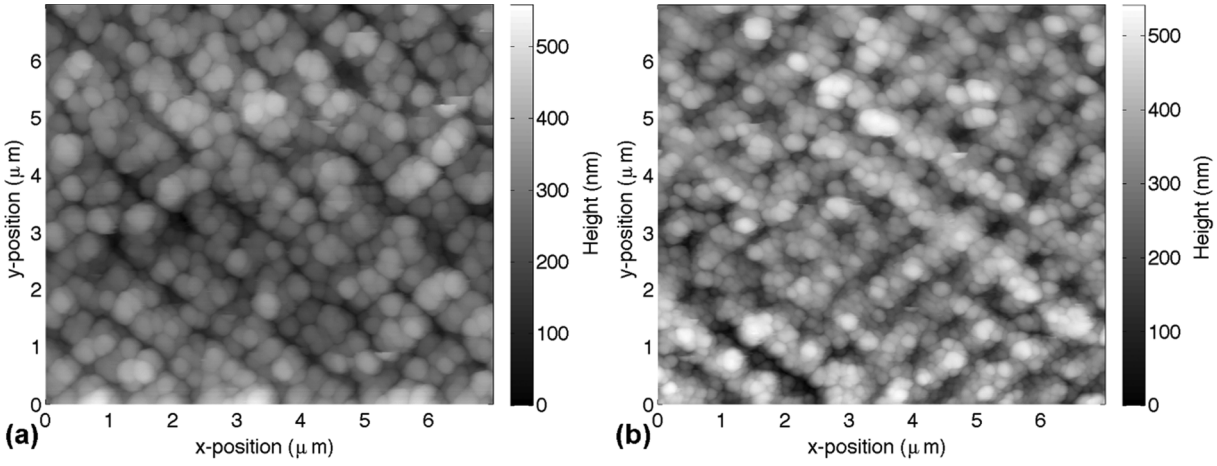

Fig. 8. ShFM topography maps of cones (a) and holes (b) structures produced by ultrashort pulsed DLIP with *p* and *s* polarization, respectively.

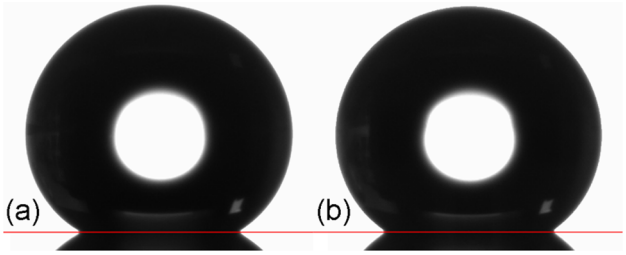

Fig. 9. Water droplet (6 µL) contact on surfaces with cones (average static water contact angle 154 ± 3°) (a) and holes (average static water contact angle 148 ± 5°) (b).

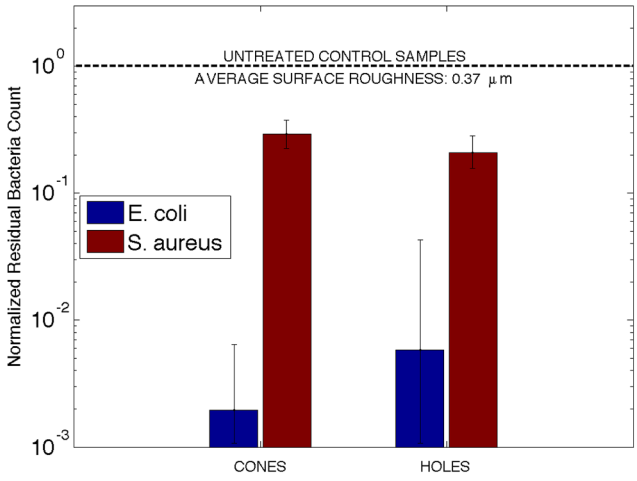

Fig. 10. Geometric averages of the residual bacterial retention for surfaces with cones and holes exposed to *E. coli* and *S. aureus* for two hours. Values are normalized against stainless steel control samples with an average surface roughness of 0.37 µm.

case, the maximum theoretical cell density (4 μm^{-2}) is greater than the density of peaks and is therefore likely to have been of lesser influence on reducing the number of attachment points. In terms of the specific surface texturing strategy, little discernable difference between cones and holes can be observed.

With both surface structure size and wettability accounted for by ultrashort pulsed DLIP, laser-textured samples exhibit good antibacterial performance for both tested cell types. It is nonetheless possible that finer surface features could further reduce the retention of *S. aureus*. Additional reductions in the dimensions of the generated structures are possible, providing scope for further investigation into DLIP for antibacterial surfaces at a wavelength of 1030 nm. Upscaling the process by optimizing laser texturing at a wavelength of 1030 nm is of fundament importance for achieving industrially relevant texturing rates. The obtained results nonetheless exhibit large improvements over current industrial practice while achieving such reductions over much larger areas than have been demonstrated to date for metallic surfaces subject to DLIP [33–37].

3.6. Application to rough stainless steel surfaces

Fig. 11 shows SEM images of cones (two process steps, *p*-polarization) and holes (one process step, *s*-polarization) applied to rough stainless steel surfaces. The images show grain boundaries with differences in height. It is clear that the structures appear at different heights if the grain boundaries are wide enough to allow interference to take place. How large the height differences can be also depends strongly on the interference volume of the overlapping beams. The smaller the volume, the smaller the height differences can be. These results nonetheless confirm applicability of the proposed DLIP texturing approach to industrially relevant surfaces.

4. Conclusion

Ultrashort pulsed DLIP has been shown to be an effective approach for producing periodic surface structures on stainless steel suitable for limiting bacterial attachment and retention over an area of 250 mm^2. Bacterial retention was shown to be reduced by up to 99.8% for *E. coli* and 70.6% for *S. aureus* through appropriate selection of the interference pattern and laser parameters. DLIP provides greater flexibility than LIPSS due to the possibility of tailoring the interference pattern to achieve specific characteristics appropriate for antibacterial surfaces. A two-beam interference line pattern and a perpendicular crosswise structuring strategy were chosen to achieve periodic 2D structures with good contrast and small periods, in the order of 850 nm with a laser wavelength of 1030 nm. Specific structure types with cones and holes were chosen not only to demonstrate their antibacterial properties, but also to highlight further potential for new applications such as negative texturing of molds for production of non-metallic components. The transfer of such surface structures through molding processes and the resulting antibacterial performance provide much scope for future work. Though smaller structures could potentially be produced by utilizing a laser source with shorter wavelength, optimization of DLIP performed at a wavelength of 1030 nm is important for upscaling to industrial throughput on large surfaces, possible through increases in average power provided by advanced laser sources currently available at this wavelength. Ultrashort pulsed DLIP will now be tested to process yet larger areas and with a greater variety of micro-organisms to

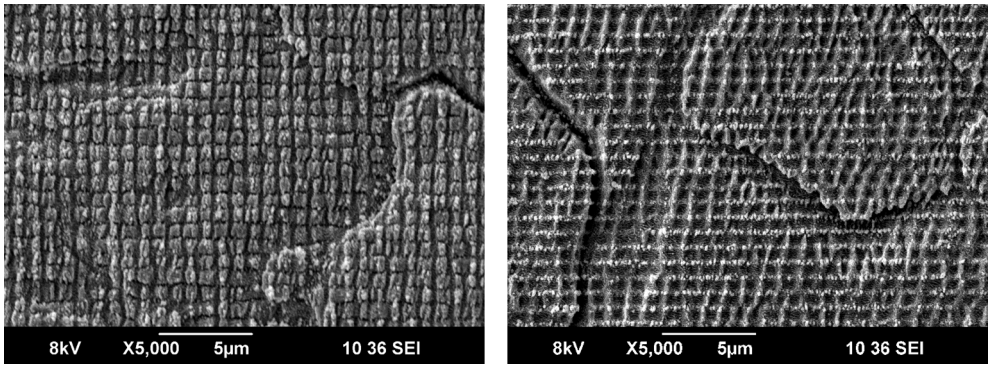

Fig. 11. SEM images of cones and holes (one laser pass) structures applied to rough stainless steel surfaces.

promote uptake in new applications in the food and healthcare industries.

Declaration of Competing Interest

The authors declare that there are no conflicts of interest.

Acknowledgements

This project has received funding from the European Union's Horizon 2020 Research and Innovation Programme under Grant Agreement No. 687613. The authors would like to thank Alessandra Carletti (Artest – Laboratori e Servizi – S.p.A.) for her assistance in developing and performing the bacterial adhesion tests.

References

[1] S. Srey, I.K. Jahid, S.-D. Ha, Biofilm formation in food industries: a food safety concern, Food Control 31 (2013) 572–585.
[2] M.A. Isaacs, L.J. Durndell, A.C. Hilton, L. Olivi, C.M.A. Parlett, K. Wilson, et al., Tunable Ag@SiO_2 core-shell nanocomposites for broad spectrum antibacterial applications, RSC Adv. 7 (2017) 23342–23347.
[3] A. Meireles, A. Borges, E. Giaouris, M. Simões, The current knowledge on the application of anti-biofilm enzymes in the food industry, Food Res. Int. 86 (2016) 140–146.
[4] D.P. Linklater, S. Juodkazis, E.P. Ivanova, Nanofabrication of mechano-bactericidal surfaces, Nanoscale 9 (2017) 16564–16585.
[5] N.A. Patankar, Mimicking the lotus effect: influence of double roughness structures and slender pillars, Langmuir 20 (2004) 8209–8213.
[6] S.M. Kelleher, O. Habimana, J. Lawler, B. O'Reilly, S. Daniels, E. Casey, et al., Cicada wing surface topography: an investigation into the bactericidal properties of nanostructural features, ACS Appl. Mater. Interfaces 8 (2016) 14966–14974.
[7] K.A. Whitehead, J. Verran, The effect of surface topography on the retention of microorganisms, Food Bioprod. Process. 84 (2006) 253–259.
[8] B.J. Privett, J. Youn, S.A. Hong, J. Lee, J. Han, J.H. Shin, et al., Antibacterial fluorinated silica colloid superhydrophobic surfaces, Langmuir 27 (2011) 9597–9601.
[9] R. Helbig, D. Günther, J. Friedrichs, F. Rößler, A. Lasagni, C. Werner, The impact of structure dimensions on initial bacterial adhesion, Biomater. Sci. 4 (2016) 1074–1078.
[10] N. Epperlein, F. Menzel, K. Schwibbert, R. Koter, J. Bonse, J. Sameith, et al., Influence of femtosecond laser produced nanostructures on biofilm growth on steel, Appl. Surf. Sci. 418B (2017) 420–424.
[11] E. Fadeeva, V.K. Truong, M. Stiesch, B.N. Chichkov, R.J. Crawford, J. Wang, et al., Bacterial retention on superhydrophobic titanium surfaces fabricated by femtosecond laser ablation, Langmuir 27 (2011) 3012–3019.
[12] F.H. Rajab, C.M. Liauw, P.S. Benson, L. Li, K.A. Whitehead, Picosecond laser treatment production of hierarchical structured stainless steel to reduce bacterial fouling, Food Bioprod. Process. 109 (2018) 29–40.
[13] A.H.A. Lutey, L. Gemini, L. Romoli, G. Lazzini, F. Fuso, M. Faucon, et al., Towards laser-textured antibacterial surfaces, Sci. Rep. 8 (2018) 10112.
[14] A.-M. Kietzig, S.G. Hatzikiriakos, P. Englezos, Patterned superhydrophobic metallic surfaces, Langmuir 25 (2009) 4821–4827.
[15] J. Bonse, S. Höhm, S.V. Kirner, A. Rosenfeld, J. Krüger, Laser-induced periodic surface structures – a scientific evergreen, IEEE J. Sel. Top. Quant. Electron. 23 (2017) 9000615.
[16] L. Gemini, M. Faucon, L. Romoli, R. Kling, High throughput laser texturing of superhydrophobic surfaces on steel, Proc. SPIE 10092 (2017) 1–6.
[17] P. Lorazo, L.J. Lewis, M. Meunier, Thermodynamic pathways to melting, ablation, and solidification in absorbing solids under pulsed laser irradiation, Phys. Rev. B 73 (2006) 134108.
[18] I. Gnilitskyi, T.J.-Y. Derrien, Y. Levy, N.M. Bulgakova, T. Mocek, L. Orazi, High-speed manufacturing of highly regular femtosecond laser-induced periodic surface structures: physical origin of regularity, Sci. Rep. 7 (2017) 8485.
[19] G.D. Tsibidis, C. Fotakis, E. Stratakis, From ripples to spikes: A hydrodynamical mechanism to interpret femtosecond laser-induced self-assembled structures, Phys. Rev. B 92 (2015) 041405(R).
[20] F. Fraggelakis, G. Mincuzzi, J. Lopez, I. Manek-Hönninger, R. Kling, Controlling 2D laser nano structuring over large area with double femtosecond pulses, Appl. Surf. Sci. 470 (2019) 677–686.
[21] E. Skoulas, A. Manousaki, C. Fotakis, E. Stratakis, Biomimetic surface structuring using cylindrical vector femtosecond laser beams, Sci. Rep. 7 (2017) 45114.
[22] J.-M. Romano, A. Garcia-Giron, P. Penchev, S. Dimov, Triangular laser-induced submicron textures for functionalising stainless steel surfaces, Appl. Surf. Sci. 440 (2018) 162–169.
[23] A. Papadopoulos, E. Skoulas, A. Mimidis, G. Perrakis, G. Kenanakis, G.D. Tsibidis, et al., Biomimetic omnidirectional antireflective glass via direct ultrafast laser nanostructuring, Adv. Mater. 31 (2019) 1901123.
[24] J. Cong, J. Yang, B. Zhao, X. Xu, Fabricating subwavelength dot-matrix surface structures of molybdenum by transient correlated actions of two-color femtosecond laser beams, Opt. Exp. 23 (2015) 5357–5367.
[25] C. Daniel, F. Mücklich, Z. Liu, Periodical micro-nano-structuring of metallic surfaces by interfering laser beams, Appl. Surf. Sci. 208–209 (2003) 317–321.
[26] B. Tan, N.R. Sivakumar, K. Venkatakrishnan, Direct grating writing using femtosecond laser interference fringes formed at the focal point, J. Opt. A: Pure Appl. Opt. 7 (2005) 169–174.
[27] A.F. Lasagni, R. Roch, D. Langheinrich, M. Bieda, A. Wetzig, Large area direct fabrication of periodic arrays using interference patterning, Phys. Procedia 12 (2011) 214–220.
[28] A. Lasagni, A. D'Alessandria, R. Giovanelli, F. Mücklich F, Advanced design of periodical architectures in bulk metals by means of laser interference metallurgy, Appl. Surf. Sci. 254 (2007) 930–936.
[29] J. Huang, S. Beckemper, A. Gillner, K. Wang, Tunable surface texturing by polarization-controlled three-beam interference, J. Micromech. Microeng. 20 (2010) 95004.
[30] A.I. Aguilar-Morales, S. Alamri, T. Kunze, A.F. Lasagni, Influence of processing parameters on surface texture homogeneity using direct laser interference patterning, Opt. Laser Technol. 107 (2018) 216–227.
[31] B. Voisiat, C. Zwahr, A.F. Lasagni, Growth of regular micro-pillar arrays on steel by polarization-controlled laser interference patterning, Appl. Surf. Sci. 471 (2019) 1065–1071.
[32] S. Alamri, F. Fraggelakis, T. Kunze, B. Krupop, G. Mincuzzi, R. Kling, et al., On the interplay of DLIP and LIPSS upon ultra-short laser pulse irradiation, Materials 12 (2019) 1–9.
[33] S. Mathews, M. Hans, F. Mücklich, M. Solioz, Contact killing of bacteria on copper is suppressed if bacterial-metal contact is prevented and is induced on iron by copper ions, Appl. Environ. Microbiol. 79 (2013) 2605–2611.
[34] D. Guenther, J. Valle, S. Burgui, C. Gil, G. Solano, A. Toledo-Arana, et al., Direct laser interference patterning for decreased bacterial attachment, Proc. SPIE 9736 (2016) 1–9.
[35] L.A. Gallarato, L.E. Mulko, M.S. Dardanelli, C.A. Barbero, D.F. Acevedo, E.I. Yslas, Synergistic effect of polyaniline coverage and surface microstructure on the inhibition of Pseudomonas aeruginosa biofilm formation, Colloids Surf., B 150 (2017) 1–7.
[36] A. Rosenkranz, M. Hans, C. Gachot, A. Thome, S. Bonk, F. Mücklich, Direct laser interference patterning: tailoring of contact area for frictional and antibacterial properties, Lubricants 4 (2016) 2.
[37] C. Zwahr, R. Helbig, C. Werner, A.F. Lasagni, Fabrication of multifunctional titanium surfaces by producing hierarchical surface patterns using laser based ablation methods, Sci. Rep. 9 (2019) 6721.
[38] P. Negel, A. Loescher, A. Voss, D. Bauer, D. Sutter, A. Killi, et al., Ultrafast thin-disk multipass laser amplifier delivering 14 kW (47 mJ, 1030 nm) average power converted to 820 W at 515 nm and 234 W at 343 nm, Opt. Exp. 23 (16) (2015) 21064, https://doi.org/10.1364/OE.23.021064.
[39] T. Nubbemeyer, M. Kaumanns, M. Ueffing, M. Gorjan, A. Alismail, H. Fattahi, et al., 1 kW, 200 mJ picosecond thin-disk laser system, Opt. Lett. 42 (2017) 1381–1384.
[40] T. Graf, High-productivity materials processing with ultrafast lasers, Journées nationales des procédés Laser pour l'industrie (2017) Strasbourg, France.
[41] B.N. Chichkov, C. Momma, S. Nolte, F. von Alvensleben, A. Tünnermann, Femtosecond, picosecond and nanosecond laser ablation of solids, Appl. Phys. A 63 (1996) 109–115.
[42] S. Preuss, A. Demchuk, M. Stuke, Sub-picosecond UV laser ablation of metals, Appl. Phys. A 61 (1995) 33–37.
[43] G. Lazzini, L. Romoli, L. Blunt, L. Gemini, Design and characterization of textured surfaces for applications in the food industry, Surf. Topogr.: Metrol. Prop. 5 (2017) 044005.
[44] J. Hofmann, S. Åkesson, G. Curiel, P. Wouters, A. Timperley, Hygienic design principles, EHEDG Guidelines, Frankfurt: European Hygienic Engineering and, 3rd ed., Design Group, 2018.
[45] A. Peter, V. Onuseit, C. Freitag, S. Faas, T. Graf. Flexible, compact and picosecond laser capable four-beam interference setup, Laser in Manufacturing (2017) Munich, Germany.
[46] M. Steger, A. Gillner, Analysis and evaluation of boundary conditions for direct surface structuring by multi-beam interference, J. Laser Micro Nanoeng. 11 (2016) 296–303.
[47] F. Tantussi, D. Vella, M. Allegrini, F. Fuso, L. Romoli, C.A.A. Rashed, Shear-force microscopy investigation of roughness and shape of micro-fabricated holes, Precis. Eng. 41 (2015) 32–39.
[48] ISO 25178 Geometrical product specifications (GPS) – Surface texture: Areal, International Organization for Standardization, 2016.
[49] J. Long, M. Zhong, H. Zhong, P. Fan, Superhydrophilicity to superhydrophobicity transition of picosecond laser microstructured aluminum in ambient air, J. Colloid Interface Sci. 441 (2015) 1–9.
[50] C. Sciancalepore, L. Gemini, L. Romoli, F. Bondioli, Study of the wettability behavior of stainless steel surfaces after ultrafast laser texturing, Surf. Coat. Technol. 352 (2018) 370–377.
[51] G. Whyman, E. Bormashenko, T. Stein, The rigorous derivation of Young, Cassie-Baxter and Wenzel equations and the analysis of the contact angle hysteresis phenomenon, Chem. Phys. Lett. 450 (2008) 355–359.
[52] J. Zimmermann, S. Seeger, F.A. Reifler, Water shedding angle: a new technique to evaluate the water-repellent properties of superhydrophobic surfaces, Text. Res. J. 79 (2009) 1565–1570.
[53] ISO 22196 Measurement of antibacterial activity on plastics and other non-porous surfaces, International Organization for Standardization, 2011.
[54] ISO 27447 Fine ceramics (advanced ceramics, advanced technical ceramics) – Test method for antibacterial activity of semi-conducting photocatalytic materials,

International Organization for Standardization, 2009.
[55] B. Neuenschwander, B. Jaeggi, M. Schmid, V. Rouffiange, P.-E. Martin, Optimization of the volume ablation rate for metals at different laser pulse-durations from ps to fs, Proc. SPIE 8243 (2012) 1–13.
[56] J.M. Liu, Simple technique for measurements of pulsed Gaussian-beam spot size, Opt. Lett. 7 (1982) 196–198.
[57] G. Raciukaitis, M. Brikas, P. Gecys, B. Voisiat, M. Gedvilas, Use of high repetition rate and high power lasers in microfabrication: How to keep the efficiency high? J. Laser Micro/Nanoeng. 4 (2009) 186–191.
[58] B. Jaeggi, B. Neuenschwander, M. Schmid, M. Muralt, J. Zuercher, U. Hunziker, Influence of the pulse duration in the ps-regime on the ablation efficiency of metals, Phys. Procedia 12 (2011) 164–171.
[59] A.Y. Vorobyev, C. Guo, Effects of nanostructure-covered femtosecond laser-induced periodic surface structures on optical absorptance of metals, Appl. Phys. A 86 (2007) 321–324.
[60] V. Lang, B. Voisiat, T. Kunze, A.F. Lasagni, Fabrication of high aspect ratio surface micro patterns on stainless steel using high-speed direct laser interference patterning, Adv. Eng. Mater. 21 (2019) 1900151.
[61] R. Weber, T. Graf, P. Berger, V. Onuseit, M. Wiedenmann, C. Freitag, et al., Heat accumulation during pulsed laser materials processing, Opt. Exp. 22 (2014) 11312–11324.
[62] D. Bergström, J. Powell, A.F.H. Kaplan, The absorptance of steels to Nd:YLF and Nd:YAG laser light at room temperature, Appl. Surf. Sci. 253 (2007) 5017–5028.
[63] K.-Y. Law, Definitions for hydrophilicity, hydrophobicity, and superhydrophobicity: getting the basics right, J. Phys. Chem. Lett. 5 (2014) 686–688.
[64] L. Feng, S. Li, Y. Li, H. Li, L. Zhang, J. Zhai, et al., Super-hydrophobic surfaces: from natural to artificial, Adv. Mater. 14 (2002) 1857–1860.
[65] Y. Arima, H. Iwata, Effect of wettability and surface functional groups on protein adsorption and cell adhesion using well-defined mixed self-assembled monolayers, Biomaterials 28 (2007) 3074–3082.
[66] C.R. Crick, S. Ismail, J. Pratten, I.P. Parkin, An investigation into bacterial attachment to an elastomeric superhydrophobic surface prepared via aerosol assisted deposition, Thin Solid Films 519 (2011) 3722–3727.
[67] A.Y. Vorobyev, C. Guo, Direct femtosecond laser surface nano/microstructuring and its applications, Laser Photon. Rev. 7 (2013) 385–407.